LANGMUIR

The ACS journal of fundamental interface science

Differences between Colloidal and Crystalline Evaporative Deposits

Samantha A. McBride,* Rachael Skye, and Kripa K. Varanasi*

Cite This: *Langmuir* 2020, 36, 11732−11741

Read Online

ACCESS | Metrics & More | Article Recommendations | Supporting Information

ABSTRACT: Evaporative deposits from drops are widely studied due to their numerous applications in low-effort self-assembly, including for inkjet printing, microscale separations, and sensing/diagnostics. This phenomenon has been broadly explored for drops containing suspended colloidal particles but has been less quantified for drops with dissolved solutes. When a drop of solute/solvent mixture is evaporated on a substrate, nonvolatile solutes become supersaturated as the solvent evaporates, which then leads to crystal nucleation at the substrate-drop contact line. Emerging crystals alter the local wettability and fundamentally alter the dynamics of evaporation, which, in turn, influences the resultant evaporative deposit. Here we investigate the role of interactions between the substrate, crystals, and solution by comparing the evaporative deposition of three different salts as solutes against an evaporating colloidal solution. We show that nucleation effects can cause crystalline deposits to have a temperature relationship that is opposite to that of colloidal deposits and demonstrate how a balance between the contact-line pinning force and nucleation controls the deposit size.
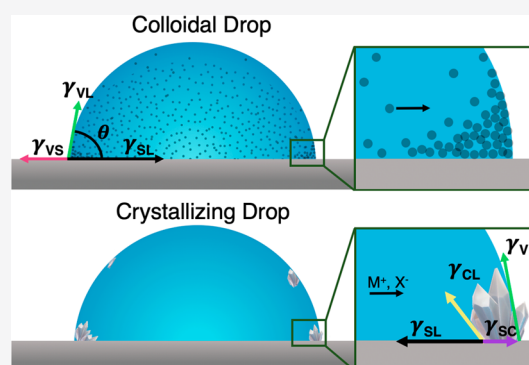
INTRODUCTION

Scientific and technological interest in evaporative self-assembly and pattern formation has proliferated rapidly since the seminal analysis of ring stains performed by Deegan et al. in 1997.[1] Since then, the evaporation of volatile solvent drops containing nonvolatile solutes has been used to engineer complex patterns ranging from rings to concentric rings,[2,3] spirals,[4,5] colloidal crystals,[3,6,7] hexagonal networks,[8] 3D shapes,[9,10] and more.[11] This facile method of producing ordered structures is attractive as an alternative to the traditional fabrication of electronics[12] and sensors[13] and can be applied to microscale separations[14] and inkjet printing.[15]

Of the 4300+ investigations citing Deegan's original "coffee-ring" paper, ~3400 cover deposition patterns formed by colloidal particles. These investigations have explored the influence of the particle shape,[16] size,[14] density,[11,17] presence of surfactants,[18,19] and interactions with the substrate and other particles.[20] External parameters including the temperature,[21] relative humidity,[22] substrate wettability,[23] heat capacities of the solute and substrate, and so on have also been explored. The deposits are typically categorized as rings, uniform deposits, or bumps.[17] The emergence of one deposit morphology over another is due to the competing interactions of evaporative flow, forces between the particles and substrate, and Marangoni recirculation.[3,16,17,24]

Despite the abundance of work exploring the evaporative self-assembly of colloids from drops, less is known regarding crystallizing solutes. In crystalline evaporative deposition, a drop containing a mixture of a solvent (usually water) and a nonvolatile solute is evaporated on a substrate. As the solvent

evaporates, the concentration of the solute increases past its solubility level so that the solute begins to precipitate. Some previous work in this area sought to use solutes in addition to colloidal particles to influence deposition patterns of the colloids. In particular, surfactants have been used in many investigations to alter the contact angle and Marangoni recirculation to suppress ring-shaped deposition.[18,19,25,26] The crystallization of sugar during evaporation was also found to lead to uniform deposition due to the crystal-induced alteration of wettability.[27] The presence of electrically charged solutes can also have an electrokinetic effect when exposed to an electric field, and thus can be used to alter deposition.[28] Importantly, the presence of salts in a colloidal drop has been shown to increase the propensity of a deposit to form a ring shape.[29]

The study of pure (i.e., without particles) crystalline evaporative deposits is motivated by the same self-assembly applications as the study of colloidal deposits and warrants additional motivation in the form of understanding and controlling device dysfunction related to crystal fouling.[30−33] Crystal fouling (also called scaling) becomes even more problematic in microdevices, where miniscule amounts of precipitate can dramatically reduce the device functional-
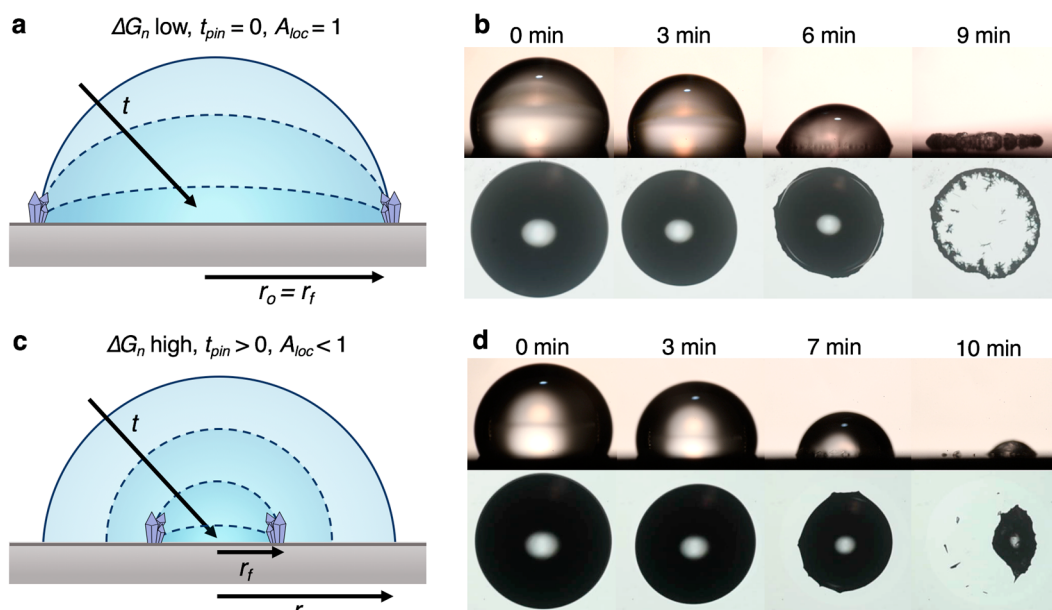
Figure 1. (a,b) Salt solutions with lower nucleation barriers will pin-drop contact lines to form rings, (c,d) whereas salts with high nucleation barriers will form lumped deposits. The experiment shown in panel b is the evaporation of a 5 μL drop of saturated calcium sulfate solution at 40 °C on a hydrophobic substrate (OTS), and panel d shows the evaporation of a 5 μL drop of saturated silver sulfate solution at 40 °C on the same hydrophobic substrate. The scale is the same for all images shown in panels b and d and is 2.8 mm across.

Table 1. Properties of Different Substrates Used in This Study, Including the Nonpolar (γ_{LW}) and Polar (γ_{AB}) Components of Surface Energy[a]

full name	abbr.	γ_{LW} (mJ/m^2)	γAB (mJ/m^2)	γ_{total} (mJ/m^2)	θ_A (deg)	θ_E (deg)	θ_R (deg)	$\Delta\theta_{AR}$ (deg)	$\Delta\theta_{ER}$ (deg)
triethoxyphenylsilane	TOPS	35.7	9.0	44.7	40	34	12	28	22
(3-aminopropyl) trimethoxysilane	AMS	34.3	2.8	37.1	57	54	31	26	23
1,2-dichlorotetramethylsilane	DTS	26.0	4.7	30.7	82	68	62	20	6
octyltrichlorosilane	OTS	22.9	0.04	22.9	112	106	98	14	8
trichloro (1H,1H,2H,2H-perfluorooctyl) silane	FS	8.7	0.03	8.7	124	110	100	24	10

[a]Advancing (θ_A), receding (θ_R), and equilibrium (θ_E) contact angles listed here are for DI water, along with the contact-angle hysteresis between the advancing and receding angle ($\Delta\theta_{AR}$) and the hysteresis between the equilibrium and receding angles ($\Delta\theta_{ER}$).

ity.[34,35] Thus understanding and controlling crystallization at interfaces is critical toward the continued development and implementation of microscale flow systems.

Previous investigations exploring crystalline evaporative deposition have demonstrated that the forces controlling deposit morphology for crystals are distinct from those that control colloidal deposits from evaporating drops.[10,32,36] Crystalline deposits will form rings even on superhydrophobic surfaces,[10] are independent of the substrate thermal conductivity,[36] and demonstrate a large dependence on the interfacial properties of the emerging crystals.[32] Additional evidence suggests that the internal convection of evaporating drops of saline solutions containing a high concentration of a highly soluble salt (NaCl, CaCl$_2$, etc.) is altered from that of pure water.[29,30,37] Specifically, the presence of solutes can reverse the direction of internal convection due to altered Marangoni stresses.[29] This solutal convective effect is a strong function of the salt concentration.[37] High salt concentrations can also influence the drop contact angle and evaporation rate, which, in turn, will influence the deposit pattern.[38,39]

Here we explore the interplay between crystallization and surface interactions in the evaporative deposition of a crystallizing solution by comparing the evaporation dynamics and the final deposit morphologies of the evaporating drops of three low-solubility salts. We use this methodology to explore how both the crystallization propensity and the substrate wettability influence the formation of crystalline deposits. Specifically, we probe the hypothesis that competition between contact-line mobility and crystallization nucleation barriers controls deposit morphologies (Figure 1). We predict that salts which crystallize readily on a given substrate will form ring deposits (Figure 1a,b), whereas salts with a higher heterogeneous nucleation barrier on a given substrate will form bump-like deposits (Figure 1c,d), This effect can be quantified via the area localization (A_{loc}, the ratio between the substrate area in contact with the initial drop (A_O) and the area of the final deposit (A_E)) and by the supersaturation at the moment of crystallization, which is directly related to the nucleation barrier. Three sparingly soluble salts were compared with a typical colloidal solution containing 1 μm latex particles to investigate the differences across salts as well as the differences between saline and colloidal drops. By using salts with lower solubilities (and therefore a smaller initial concentration), we seek to limit alterations to the surface tension, evaporation rate, and internal convection associated with high salt concentrations.[38−40] We confirm that both area localization and
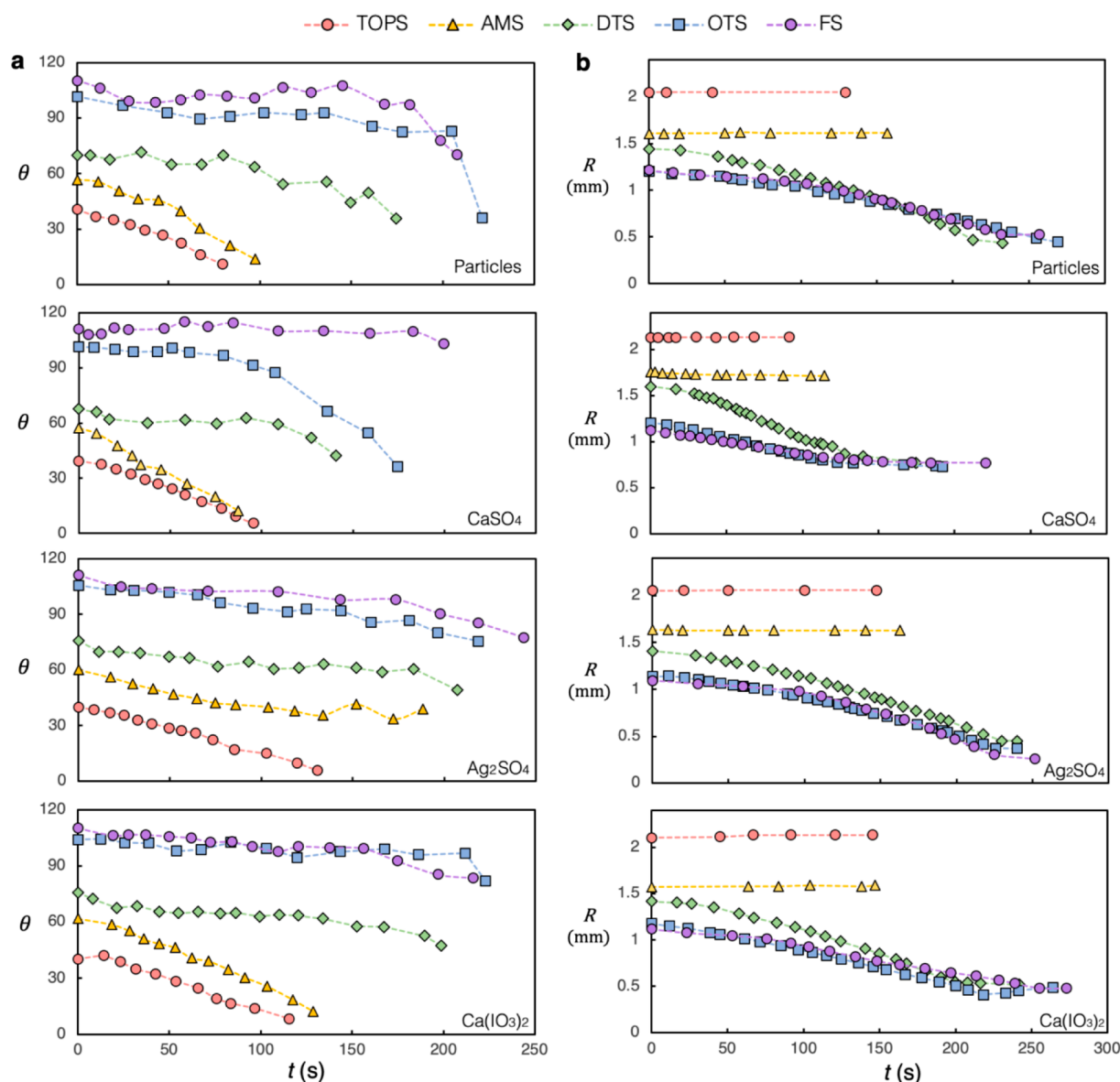
Figure 2. Drop evaporation as a function of time. (a) Contact angle, θ (degrees), over time for different solutions at 60 °C. Contact-angle measurements were terminated at the point at which the contact line became too distorted by particle/crystal accumulation to extract an angle. (b) Drop contact radius over time for the different solutions at 60 °C.

supersaturation at the moment of crystallization are indeed altered across substrates and demonstrate that supersaturation is a controlling factor in the deposit shape.

MATERIALS AND METHODS

Surface Preparation. Silicon wafers (or glass slides) were functionalized with the silane groups listed in Table 1 to create a range of wetting properties. Their preparation has been previously described.[41] For the oxysilanes (triethoxy-phenylsilane (TOPS) and (3-aminopropyl) trimethyoxysilane (AMS)), plasma-cleaned silicon substrates were added to a mixture of 0.075% hydrochloric acid in ethanol. Silane was added to 0.2% (volume) concentration, and beakers were capped and left to react for at least 24 h. Two other silanized substrates (1,2-dichloro-tetramethyl-silane (DTS) and octyl-trichlorosilane (OTS)) were prepared using a different liquid deposition method in which plasma-cleaned substrates are added to a reaction beaker with 30 mL of toluene and 75 μL of silane. In a separate beaker, an emulsion of 20 mL of toluene and 100 μL of DI water was prepared. This emulsion was poured into the reaction beaker, and substrates were sonicated for 4 min to facilitate the

reaction. Substrates were then rinsed with acetone and isopropyl alcohol to remove excess silane. The fluorosilane substrates (trichloro (1H,1H,2H,2H-perfluorooctyl) silane (FS)) were prepared via vapor deposition. Plasma-cleaned substrates were placed in a desiccator alongside a small drop of silane solution. The chamber was vacuumed and left for a period of at least 8 h for complete reaction. Samples were stored in airtight containers and used within 1 month of preparation.

Solution Preparation. Evaporative deposits for three different saline solutions were compared with deposits from a typical colloidal solution in these experiments. Calcium sulfate, silver sulfate, and calcium iodate were purchased as solids from Sigma-Aldrich. Salts were added to DI water at a concentration in excess of their solubility limits and allowed to mix and dissolve for a period of at least 18 h at ambient temperature before excess solid was filtered out to leave a particle-free, saturated salt solution. The relatively low saturation concentration of these sparingly soluble salts did not cause significant changes to the evaporation rate or the drop contact angle. (See the SI for evaporation rates.) These particular salt solutions were chosen specifically for their solubility properties (see the SI for the solubility
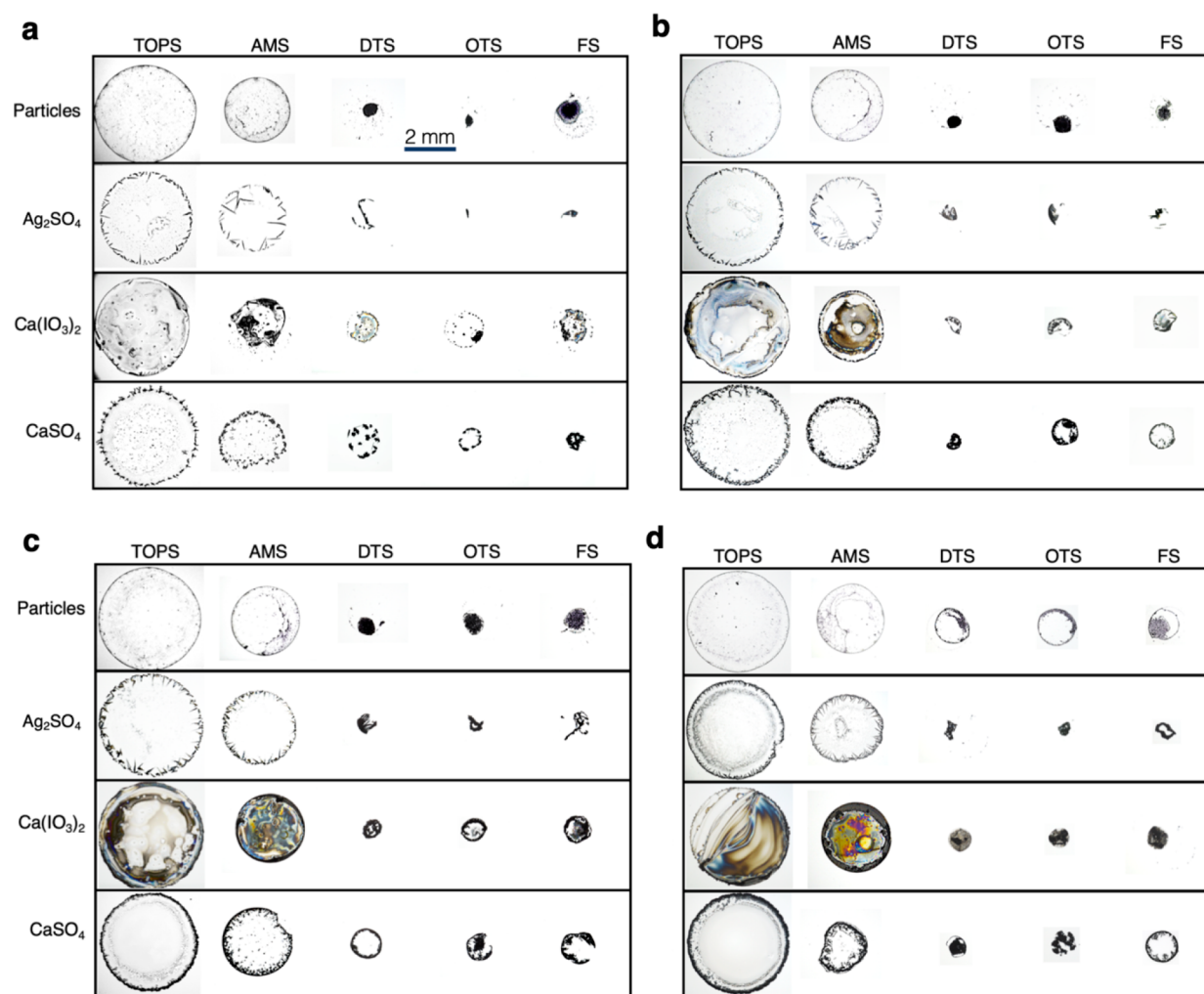
Figure 3. Representative patterns from experiments for (first row) particles, (second row) silver sulfate, (third row) calcium iodate, (fourth row) calcium sulfate. (a) 20, (b) 40, (c) 60, and (d) 80 °C. Length scale is the same for all images.

table), which are on the same order of magnitude across the three solutions and fall into the upper range of the sparingly soluble category. By comparing three salts with similar saturation concentrations, we attempt to eliminate concentration effects as much as possible to better compare the crystallization behavior.

Latex particles of 1 μm diameter were added to DI water at a concentration of 0.1% V/V to create the colloidal solution. The coffee-ring behavior of colloidal solutions is highly dependent on the particle size, shape, chemistry (in particular, how that chemistry affects particle–particle and substrate/particle attraction), and concentration. The present formulation was chosen as a standard solution that can form either rings or lumped deposits under the experimental conditions used here.

Surface Characterization. A goniometer was used to characterize substrate contact angles. Three different probe liquids (water, ethylene glycol, and diiodomethane) were used to extract the different components of surface energy listed in Table 1. These measurements were conducted in triplicate and were repeated each time a new batch of substrates was prepared. For XPS spectra of substrates prepared, see Azimi et al. 2014.[41] Dynamic (θ_A, θ_R) and equilibrium (θ_E) contact angles were measured for each surface using DI water. As previously noted, the low saturation concentration of the salts used here is not predicted to have a significant influence on the wetting properties measured for DI water, and the experimental results confirm that no significant deviations are observed. The contact-angle hysteresis is typically defined as the difference between the advancing and receding angles. However, we have also included the hysteresis

between the equilibrium (also referred to as the Young angle) and the receding angles, which will be more relevant for characterizing the present experiments, where the initial state of the drop is the equilibrium angle.

Experiments. Experiments were conducted by heating the functionalized substrates to a controlled temperature (20, 40, 60, or 80 °C) and depositing 5 μL drops of the saline or particle-laden solution. Experiments were conducted in a temperature-regulated lab under ambient conditions (temperature of 20 °C) at a relative humidity range between 38 and 45%. Control experiments published elsewhere have shown that this range of RH values does not alter experimental results in terms of the evaporation rates or deposit contact area.[10] Evaporation was recorded using a Zeiss microscope equipped with a Nikon D300 camera from the top, and side views to capture contact-angle dynamics were recorded using a Nikon D800 equipped with a Navitar lens. Experiments at elevated temperatures were repeated between three and six times per sample, and information on standard deviations for measurements along with evaporation rate data is available in the Supporting Information (SI).

Data Analysis. The resultant videos were processed to extract the following parameters: time until crystallization (t_c), total evaporation time (t_E), contact area between the drop and the substrate at first deposition (A_o), initial contact angle (θ_o), contact angle and contact area at the first appearance of crystals (θ_c, A_c), contact angle as a function of time, and final area covered by the resultant deposit after complete evaporation (A_E). For noncircular final deposits (which occurred frequently for silver sulfate deposits; see Figure 3), the
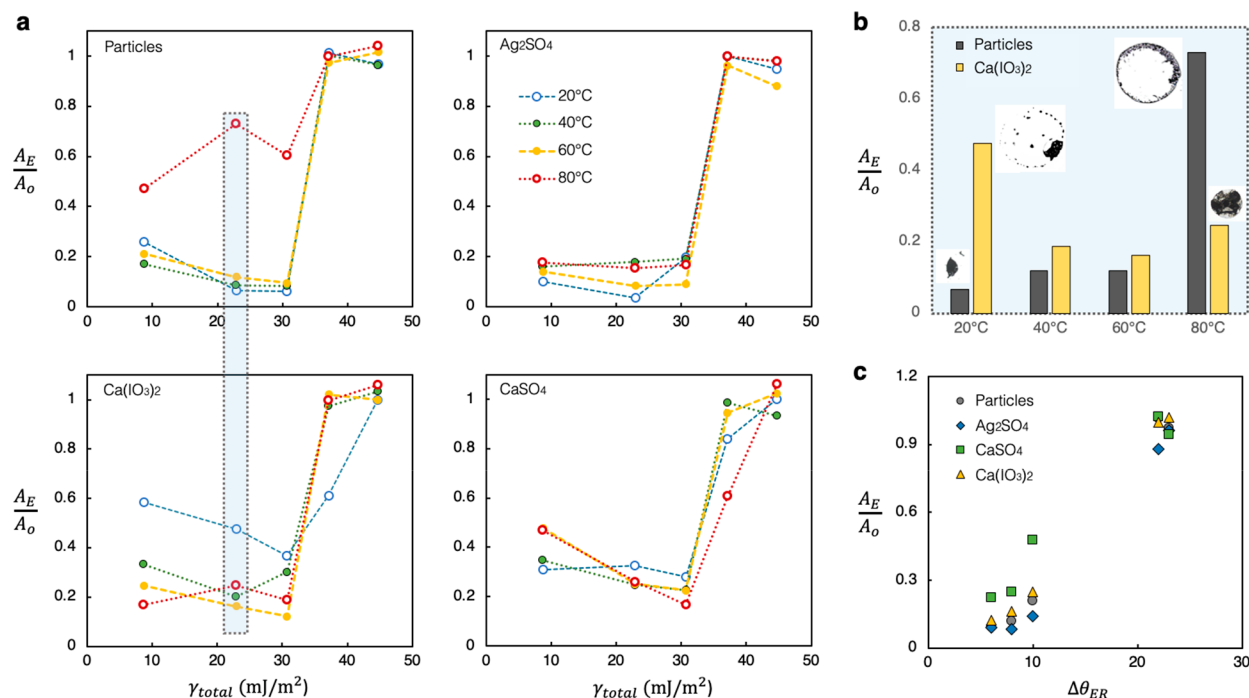
Figure 4. (a) Area localization (ratio of the final contact area of deposit to the contact area of initial drop) as a function of substrate surface area (where the more wettable substrates have a higher energy) across temperatures. Standard deviations for these measurements can be found in the SI. (b) Bar graph for OTS data outlined in blue in panel a, comparing the temperature dependence of the particles and the calcium iodate deposits. (c) Area localization as a function of the contact-angle hysteresis (between the equilibrium angle and the receding angle) at 60 °C.

"diameter" of the resultant deposit was taken as the average between the longest dimension and the shortest dimension. Images of crystals (see the SI) were taken using a Zeiss Ultra55 FESEM apparatus.

RESULTS

In the classic case of an evaporating colloidal drop, evaporation typically proceeds in one of two modes: constant contact angle (cca) or constant contact radius (ccr).[42,43] Constant contact angle means that the drop contact area decreases with time as the contact line slides over the substrate, leaving a condensed deposit. In constant contact radius evaporation, the drop contact line remains pinned to the substrate, and the contact angle decreases with time. Other modes of contact-line dynamics during evaporation include stick–slip motion,[44,45] rapidly receding "rupture" motion, and slow recession, where the contact angle and radius change simultaneously.[46] Stick–slip behavior is frequently observed for evaporating colloidal drops and is dependent on the concentration of particles.[47]

When a colloidal drop is replaced by a saline drop, the contact-line dynamics become somewhat more complicated as both the wetting properties and the supersaturation of the salt change with time. Rather than accumulating particles at the triple contact line due to outward radial flow, the supersaturation of salt increases at the contact line where ions are unable to follow water into the vapor phase. This leads to crystallization in the vicinity of the contact line, which may then influence pinning of the contact line. Pinning will be enhanced when crystals adhere to the substrate and will fundamentally alter the receding contact angle due to the altered wettability caused by crystal formation.[27] These sparingly water-soluble crystals are typically hydrophilic and thus tend to enhance the pinning by increasing the substrate wettability. However, crystallization will not always lead to drop pinning.[36] When crystals do not adhere to the underlying

substrate, they will sometimes be "dragged" along by the motion of the contact line to form a clumped deposit rather than a ring.

Figure 2a shows the change in contact angle over time during the evaporation of drops at 60 °C on the different substrates, whereas Figure 2b shows the contact radius with time. The top left panel shows the control case using a colloidal drop. For the two most hydrophobic surfaces (OTS and FS), the drop evaporates with a relatively constant contact angle (cca mode) until the very end of the evaporation process, when the contact line becomes pinned due to increasing concentrations of particles. This suggests that a highly condensed deposit will form (see Figure 3c, last two columns). This trend also follows for two of the salt solutions, calcium iodate and silver sulfate. However, for calcium sulfate, we see that the contact angle of the drop on the OTS surface begins dropping about halfway through the experiment. We see in Figure 2b that this change in contact angle corresponds to pinning of the contact line and a transition to constant contact radius mode. The two most hydrophilic substrates (TOPS and AMS) show relatively little difference across the different solutions, in that they all occur in constant contact radius mode and thus leave ring deposits (Figure 3c, first two columns).

Although the DTS substrate has an initial contact angle that is only somewhat higher than that of the AMS substrate, the low contact-angle hysteresis between the equilibrium angle and the receding angle of DTS (6° compared with 23° for the AMS substrate) leads to significant contact-line motion. The contact-line dynamics for this surface demonstrates a mixed mode where both the contact angle and the contact radius decrease with time for all solutions except calcium sulfate, where we once again see a transition in modes.

The results of Figure 2 hint at some differences between the evaporative modes for saline and colloidal drops. The outcomes of these differences are shown in Figure 3, which shows representative patterns from experiments at 20 (Figure 3a), 40 (Figure 3b), 60 (Figure 3c), and 80 °C (Figure 3d). As expected, the hydrophilic substrates (TOPS and AMS, $\theta_E = 34$ and 54°, respectively) form ring patterns across temperatures and solutions. At very high evaporation rates (80 °C), particles leave behind ring-shaped deposits, even on the most hydrophobic surfaces. This is an expected and previously observed result and can be attributed to the internal evaporative flow exceeding the Marangoni recirculation, which acts to move particles toward the drop center.[17,23,48] In contrast, the deposits left by calcium iodate on the hydrophobic surfaces are ring-like at 20 °C and become more condensed with increasing temperature.

A notable result of Figure 3 is the lack of influence of temperature on calcium sulfate and silver sulfate. Changing the temperature does not seem to significantly alter deposits formed for either solution. However, the two do not exhibit the same behavior. We see that drops tend to pin at the onset of the crystallization for calcium sulfate, whereas for silver sulfate, the contact line continues to move even once crystals have begun to form. The result is that calcium sulfate deposits tend to be ring-shaped across temperatures and substrates, whereas silver sulfate deposits tend to be a clumped gathering of individual crystals. (See the SI for SEM images that show representative crystals.)

An expected result shown in Figure 3 is the relationship between the evaporation rate and the crystal growth. At low temperatures, fewer crystals nucleate, and those crystals grow larger. At higher temperatures, more crystals nucleate, and those crystals do not grow to large sizes. This trend is particularly apparent among silver sulfate deposits. (The selected image shown for silver sulfate on OTS at 20 °C is a single crystal. Note that the mass is constant across all experiments and that this single crystal is significantly larger in the vertical direction than the other silver sulfate crystals shown across other deposits.)

A quantitative method of describing the deposit morphology is the area localization, which is the ratio of the initial contact area between the drop and the substrate to the final area of the resultant deposit. This dimensionless ratio is a more useful metric than the dimensional area because it gives an indication of the contact-line motion during evaporation. For a drop that remains pinned and evaporates in a constant contact radius mode, this ratio will be 1, as the initial area of the drop and the final area of the deposit will be the same. The resulting deposit for such a drop will typically be a ring, especially for crystalline deposits where crystals tend to nucleate at contact lines. For a drop evaporating in constant contact-angle mode with constant recession of the contact line, the resultant deposit will be highly condensed compared with the initial area, leading to a smaller ratio. The area localization will be some intermediate value for a drop that begins evaporation in cca mode but transitions to ccr mode due to pinning. This ratio has been plotted as a function of the substrate surface energy (see Table 1; higher surface energy = more hydrophilic) in Figure 4a across temperatures for each of the four solutions.

Comparing the area localization data of Figure 4a across calcium iodate and particles confirms the observation from Figure 3 that the two solutions exhibit opposite trends with temperature. This trend reversal is highlighted in Figure 4b,

which displays data for the OTS surface (i.e., the points highlighted in blue in Figure 4a). The calcium iodate deposits are largest at the lowest temperature and form a ring shape. At the highest temperature of 80 °C, the calcium iodate deposit is clumped. This result is in line with predictions from a previous molecular dynamics investigation, which found that sodium chloride is more likely to form rings under slow evaporation conditions.[39] In contrast, the particle deposit is the largest (and ring-shaped) at 80 °C and is clumped at 20 °C.

In general, deposits on lower surface energy (more hydrophobic) substrates have a lower area localization. However, we see that the area localization on the most hydrophobic surfaces (FS, $\gamma_{total} = 8.7$ mJ/m^2) is often higher than it is for the OTS or DTS surfaces ($\gamma_{total} = 22.9$ and 30.7 mJ/m^2, respectively). This effect is particularly pronounced for the calcium sulfate deposits (bottom right of Figure 4a). Unlike the absolute deposit area presented in Figure 3, the area localization is a function of the contact-line dynamics. This means, for example, that a hydrophilic substrate with low contact-angle hysteresis can form a deposit with a relatively large physical size but small area localization and that a deposit on a hydrophobic substrate with high contact-angle hysteresis can have a small size but large area localization. Thus area localization has a strong dependence on the contact-angle hysteresis between the equilibrium angle and the receding angle (Table 1, last column), as shown in Figure 4c.

For calcium sulfate deposits, the minimum area localization occurs on the DTS surface ($\gamma_{total} = 30.7$ mJ/m^2), which also has the lowest contact-angle hysteresis ($\Delta\theta_{ER} = 6°$). Similarly, whereas FS exhibits the largest overall contact angle, the calcium sulfate deposits on the FS surface have the largest area localization of the three hydrophobic surfaces. This is likely due to the slightly higher contact-angle hysteresis ($\Delta\theta_{ER} = 10°$). The trend is most apparent for the calcium sulfate deposits (see the bottom left of Figure 4a) but also holds well across solutions. Figure 4c compares this relationship for deposits formed at 60 °C. The observation that the area localization of the calcium sulfate deposits is more sensitive to contact-angle hysteresis than other solutions (in particular, silver sulfate) suggests that burgeoning calcium sulfate crystals pin the receding interface more readily than silver sulfate crystals, which is indeed observed (see Figure 2; calcium sulfate deposits are more likely to form rings than silver sulfate).

■ DISCUSSION

We have shown that crystallizing solutes do not behave the same as a colloidal solution (silver sulfate and calcium sulfate do not demonstrate a significant temperature dependence) and that calcium iodate, in particular, demonstrates the reverse trend of the colloidal solution (where the colloidal solution is more likely to form rings at high evaporation rates and calcium iodate forms condensed deposits at high evaporation rates). Now we consider how the interplay between crystal nucleation and substrate contact-line dynamics can explain this behavior.

In Figure 4c, we observed that the area localization could be correlated to the substrate contact-angle hysteresis, which hints at the importance of contact-line pinning. However, crystallization also plays a role, as evidenced by the difference in the area localization across salt solutions. Calcium sulfate, the salt most likely to form ring deposits, exhibits the largest area localization for a given contact-angle hysteresis, whereas silver sulfate and calcium iodate exhibit lower area localization and
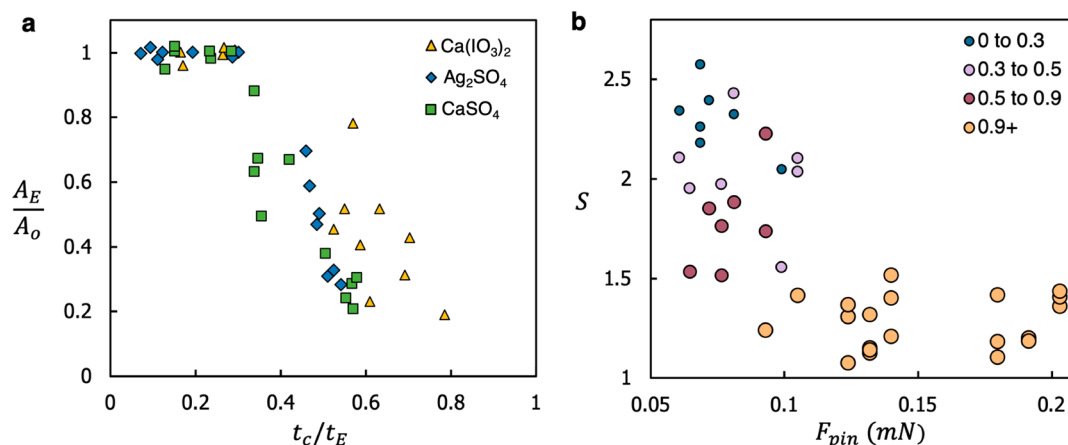
Figure 5. Data across five substrates and three temperatures (40, 60, and 80 °C) collapse onto a single trend based on the supersaturation at crystal nucleation. (a) Squares = calcium sulfate, diamonds = silver sulfate, triangles = calcium iodate. (b) Phase diagram of the pinning force against the supersaturation, where $F_{pin} = 2\pi R\gamma(T)(\cos\theta_R - \cos\theta_A)$, S_c is from experimental data, estimated as $S_c = V_o/V_c$, and data are classified according to the area localization. Data is from experiments conducted at 40, 60, and 80 °C.

are more likely to form condensed deposits. To explore the role of crystallization in contact-line pinning and therefore area localization, we plot the ratio between the crystallization time (t_c) and the total evaporation time (t_E) against the area localization (Figure 5a). This time scale ratio gives an indication of how readily the crystals form, where a lower ratio indicates that crystals emerge relatively early in the process and a higher ratio indicates that crystals begin to emerge later.

Comparing the results of Figure 5a across the three solutions shows that for a given area localization, calcium sulfate and silver sulfate crystals generally emerge earlier in the evaporation process than calcium iodate crystals. This trend might be explained by the changing solubilities with temperature. The three salts used in this study were chosen for having solubilities within the same order of magnitude to reduce concentration-induced variations. However, they do not all exhibit the same change in solubility with temperature (See Table S1 in the Supporting Information). Calcium sulfate exhibits very little change in solubility with temperature, whereas the solubility of silver sulfate increases by 1.7 times between 20 and 80 °C. Calcium iodate has a 3 times increase in solubility between the same temperatures. This difference in solubility with temperature allows us to understand the trend observed in Figure 4b, where calcium iodate formed the most localized deposits at the highest temperature. Although increased temperature increases the evaporation rate and therefore increases the rate at which ions accumulate at the contact line, the relative supersaturation for calcium iodate also decreases. In contrast, calcium sulfate does not become more soluble with temperature; therefore, the supersaturation is only a function of the evaporated volume of the drop. This result confirms that supersaturation is an essential variable in crystalline coffee-ring formation.

To explain the importance of supersaturation and its relationship to crystal nucleation induction, we consider the thermodynamics of the process. The Gibbs free-energy barrier for nucleation of a crystal can be found from classical nucleation theory, in which the Gibbs free energy of formation is the sum of a negative energy change due to the formation of solid mass and a positive energy change due to the formation of a new interface. The free-energy barrier is found as the

maximum change energy at some critical radius representing the largest barrier that must be overcome for a growing nucleus to continue growth. Assuming a hemispherical crystal nucleus forming in a substrate, this critical energy barrier is[49,50]

$$\Delta G_{n,\text{het}}^{*} = \frac{\pi V_m^2}{3(k_B T \ln S)^2}(2\gamma_{CL} + \gamma_{SC} - \gamma_{SL})^3 \quad (1)$$

where V_m is the molecular volume, k_B is the Boltzmann constant, T is the temperature, S is the supersaturation, γ_{SC} is the surface energy between the substrate and the crystal, γ_{LC} is the energy between the liquid and the crystal, and γ_{SL} is the energy between the substrate and the liquid. (For the full derivation and an explanation of eq 1, see the SI.) Thus, the energetics between the three phases (substrate, crystal, and liquid) all contribute to the nucleation barrier. Isolating values for these parameters is challenging, and it is difficult to say whether interactions between the substrate and crystal (captured by γ_{SC}) significantly influence the present results. However, it is straightforward to obtain values for the supersaturation at the onset of crystallization. Although there will be some concentration polarization within the solution (i.e., higher salt concentrations at the air/water interface due to evaporation), rapid convection and mixing enables us to estimate an average concentration within the drop and an average supersaturation (S) as a function of the drop volume (see the SI for more on convection)

$$S = \frac{C(t)}{C_{\text{sat}}} = \frac{V_o}{V(t)} \quad (2)$$

where, as previously noted, the value of C_{sat} is a function of temperature. We are particularly interested in salt supersaturation within the drop at the moment at which crystals first begin to form (and become visible under the microscope), t_c. Under conditions where the nucleation barrier is exceedingly small, crystals may begin to nucleate soon after the solution becomes supersaturated. In contrast, when the nucleation barrier is high, the solution can become highly supersaturated before crystals begin to emerge. Previous work has shown that the supersaturation of calcium sulfate can reach values of 6 or higher on surfaces with no heterogeneous nucleation sites before crystals start to form.[10]

With supersaturation as a metric to quantify the crystallization propensity (where the onset of crystallization at a low value of S_c indicates a high propensity of crystallization and a high value indicates a low propensity), we now define a metric to quantify contact-line dynamics. An appropriate choice is the pinning force, which is a function of both the equilibrium (θ_E) and receding (θ_R) angles of the surface[51]

$$F_P = 2\pi r_o \gamma (\cos \theta_R - \cos \theta_E) \tag{3}$$

where γ is the surface tension of water, 72 mJ/m^2, at 20 °C (66 mJ/m^2 at 60 °C) and r_o is the radius of the initial contact line. This equation gives the force required for depinning of the contact line. When the contact angle hysteresis is zero, there is no resistance to contact-line motion. Plotting the pinning force of eq 3 (where contact angles are taken as values shown in Table 1 and surface tension is taken as a function of temperature) against the supersaturation at crystallization (S_c) yields the diagram shown in Figure 5b. In this diagram, the area localization of the deposits has been separated into four categories: highly condensed (A_E/A_C = 0 to 0.3), condensed (A_E/A_C = 0.3 to 0.5), some reduction (A_E/A_C = 0.5 to 0.9), and nonreduced (A_E/A_C > 0.9). Higher pinning forces and high crystallization propensity result in nonreduced (and ring-shaped) deposits, whereas highly reduced deposits occur at the lowest pinning forces and the lowest propensities for crystallization.

The results of Figure 5b show that, in general, a crystal deposit will be ring-shaped and nonlocalized when crystallization occurs before the volume reduces enough to overcome the substrate pinning force. However, crystallization does not always pin the interface and impede contact-line mobility. In some cases, we see crystallization at the contact line, and yet the line continues to recede. This is particularly true for the silver sulfate experiments, in which crystals form but do not always pin the contact line. Instead, these silver sulfate crystals move with the contact line to form condensed deposits. It is here where we believe (but cannot quantify) that γ_{SC} shown in eq 1 contributes to the deposit morphology. (See Figure S1 in the Supporting Information explaining the analogy between the Young's equation for a drop on a substrate and a crystal forming on a surface). Crystals that preferentially interact with the substrate will grow on that substrate and therefore pin the contact line. Crystals without strong interactions with the substrate will still form at the contact line due to the concentration polarization as a consequence of evaporation but will not be adhered to the substrate (i.e., they will exist in the bulk). Such nonadhered crystals may move with the contact line as it recedes. Such an effect has also been observed in experiments for colloidal solutions as a function of the particle surface tension.[24]

We have seen that crystalline patterns differ from colloidal patterns deposited from an evaporating drop under the same conditions and have demonstrated that area localization is correlated with the supersaturation (and therefore the nucleation barrier) at which crystals begin to form. We now briefly consider the hypothesis that saline-induced convection, which has been previously shown to strongly alter the interior flow of the drop,[29,30,37] influences these results. Recent work has demonstrated that the salt-induced Marangoni flow can significantly increase (double or more) the rate of the deposition of colloidal particles at the contact line during coffee-ring evaporation.[29] The effect of solutal convection is more difficult to quantify here, as the effect of saline flow cannot be decoupled from the deposition of crystals at the contact line. However, we can infer from this result that Marangoni flow likely elevates supersaturation at the contact line beyond the concentration that would exist from evaporative flow alone. A higher supersaturation leads to faster nucleation, a higher likelihood of contact-line pinning due to crystallization, and more mass accumulation at the contact line. Thus, the influence of Marangoni convection in crystalline coffee-ring formation is likely the opposite of the influence of Marangoni convection in colloidal deposits. For colloidal solutions, recirculation leads to a greater deposition of particles in the interior of the drop and increases the likelihood of a lumped deposit, whereas the Marangoni flow in saline solutions transports more salt to the contact line and thus increases the likelihood of a ring deposit.

■ CONCLUSIONS

The contact-line dynamics and the evaporative crystallization from a drop both depend on the same parameters, namely, the evaporation rate and the surface energy of the substrate. We have explored the relationship between the two and demonstrated that the supersaturation at the onset of crystallization (which is directly related to the crystallization nucleation barrier) can explain the different deposit morphologies across the various solutions/substrates. Previous work exploring this relationship has shown that crystalline deposits are highly dependent on the wettability properties of the crystals and substrates.[36] We confirm this dependence here and have also demonstrated that crystalline deposits are dependent on the nucleation energy barrier. This energetic barrier is largely dependent on the wettability properties but is also dependent on the evaporation rate due to the supersaturation term. The phase diagram we develop can be used to understand how the morphology of crystalline evaporative deposits can be controlled or to understand/control the mechanisms of crystal fouling associated with wetting/evaporation cycles.

In addition to exploring the fundamental relationship between wetting, evaporation, and crystallization, we have also elucidated important differences between colloidal and crystalline evaporative deposition. Supersaturation is an essential parameter for the prediction of crystalline deposit morphology, and we have shown that altered solubility with temperature can cause crystalline deposits to have a temperature relationship inverse to the one for colloidal deposits. Another difference is the role of Marangoni circulation, which promotes localized deposits in colloidal deposition patterns. In contrast, we have seen no evidence that convective flows redistribute crystals toward the drop interior. Based on previous results,[36] if Marangoni flow plays any role in crystalline evaporative deposits, it instead may act to promote ring formation. These differences between solutal and colloidal evaporative deposition demonstrate that the two related processes are nevertheless controlled by different physics and highlight the need for the further study of the many complex factors that contribute to the crystalline evaporative assembly.

■ ASSOCIATED CONTENT

ⓢ Supporting Information

The Supporting Information is available free of charge at https://pubs.acs.org/doi/10.1021/acs.langmuir.0c01139.

Tables of crystal properties and discussion of the properties of the salts used in this study. Experimental data on evaporation rates, area localization data, and pinning force calculations. Calculations for dimensionless numbers predicting the strength of convection in these experiments and notes on how convection influenced the results. Detailed derivation of eq 1. Discussion f crystal morphologies and selected SEM images of the individual crystals that comprise the evaporative deposits (PDF)

■ AUTHOR INFORMATION

Corresponding Authors

Kripa K. Varanasi − *Department of Mechanical Engineering, Massachusetts Institute of Technology, Cambridge, Massachusetts 02139, United States;* ⓞ orcid.org/0000-0002-6846-152X; Email: varanasi@mit.edu

Samantha A. McBride − *Department of Mechanical Engineering, Massachusetts Institute of Technology, Cambridge, Massachusetts 02139, United States;* ⓞ orcid.org/0000-0002-6402-1359; Email: smcbride2@princeton.edu

Author

Rachael Skye − *Department of Materials Science Engineering, Massachusetts Institute of Technology, Cambridge, Massachusetts 02139, United States*

Complete contact information is available at:
https://pubs.acs.org/10.1021/acs.langmuir.0c01139

Author Contributions

All authors contributed to the experiments presented here and to the preparation of this manuscript.

Notes

The authors declare no competing financial interest.

■ REFERENCES

(1) Deegan, R. D.; Bakajin, O.; Dupont, T. F.; Huber, G.; Nagel, S. R.; Witten, T. A. Capillary Flow as the Cause of Ring Stains from Dried Liquid Drops. *Nature* **1997**, *389* (6653), 827−829.

(2) Xu, J.; Xia, J.; Hong, S. W.; Lin, Z.; Qiu, F.; Yang, Y. Self-Assembly of Gradient Concentric Rings via Solvent Evaporation from a Capillary Bridge. *Phys. Rev. Lett.* **2006**, *96* (6), No. 066104.

(3) Marín, Á. G.; Gelderblom, H.; Lohse, D.; Snoeijer, J. H. Order-to-Disorder Transition in Ring-Shaped Colloidal Stains. *Phys. Rev. Lett.* **2011**, *107* (8), No. 085502.

(4) Chen, Y.-J.; Suzuki, K.; Mahara, H.; Yoshikawa, K.; Yamaguchi, T. Self-Organized Archimedean Spiral Pattern: Regular Bundling of Fullerene through Solvent Evaporation. *Appl. Phys. Lett.* **2013**, *102* (4), No. 041911.

(5) McBride, S. A.; Dash, S.; Khan, S.; Varanasi, K. K. Evaporative Crystallization of Spirals. *Langmuir* **2019**, *35* (32), 10484−10490.

(6) Paria, S.; Ghosh Chaudhuri, R.; Jason, N. N. Self-Assembly of Colloidal Sulfur Particles on a Glass Surface from Evaporating Sessile Drops: Influence of Different Salts. *New J. Chem.* **2014**, *38* (12), 5943−5951.

(7) Prevo, B. G.; Velev, O. D. Controlled, Rapid Deposition of Structured Coatings from Micro- and Nanoparticle Suspensions. *Langmuir* **2004**, *20*, 2099−2107.

(8) Gonuguntla, M.; Sharma, A. Polymer Patterns in Evaporating Droplets on Dissolving Substrates. *Langmuir* **2004**, *20*, 3456−3463.

(9) Shin, B.; Moon, M.-W.; Kim, H.-Y. Rings, Igloos, and Pebbles of Salt Formed by Drying Saline Drops. *Langmuir* **2014**, *30* (43), 12837−12842.

(10) McBride, S. A.; Dash, S.; Varanasi, K. K. Evaporative Crystallization in Drops on Superhydrophobic and Liquid-Impregnated Surfaces. *Langmuir* **2018**, *34* (41), 12350−12358.

(11) Deegan, R. D. Pattern Formation in Drying Drops. *Phys. Rev. E: Stat. Phys., Plasmas, Fluids, Relat. Interdisc. Top.* **2000**, *61* (1), 475−485.

(12) Vakarelski, I. U.; Chan, D. Y. C.; Nonoguchi, T.; Shinto, H.; Higashitani, K. Assembly of Gold Nanoparticles into Microwire Networks Induced by Drying Liquid Bridges. *Phys. Rev. Lett.* **2009**, *102* (5), No. 058303.

(13) Wilson, S. A.; Jourdain, R. P. J.; Zhang, Q.; Dorey, R. A.; Bowen, C. R.; Willander, M.; Wahab, Q. U.; Willander, M.; Al-hilli, S. M.; Nur, O.; Quandt, E.; Johansson, C.; Pagounis, E.; Kohl, M.; Matovic, J.; Samel, B.; van der Wijngaart, W.; Jager, E. W. H.; Carlsson, D.; Djinovic, Z.; Wegener, M.; Moldovan, C.; Iosub, R.; Abad, E.; Wendlandt, M.; Rusu, C.; Persson, K. New Materials for Micro-Scale Sensors and Actuators: An Engineering Review. *Mater. Sci. Eng., R* **2007**, *56* (1−6), 1−129.

(14) Wong, T.-S.; Chen, T.-H.; Shen, X.; Ho, C.-M. Nanochromatography Driven by the Coffee Ring Effect. *Anal. Chem.* **2011**, *83* (6), 1871−1873.

(15) He, P.; Derby, B. Controlling Coffee Ring Formation during Drying of Inkjet Printed 2D Inks. *Adv. Mater. Interfaces* **2017**, *4*, 1700944.

(16) Yunker, P. J.; Still, T.; Lohr, M. A.; Yodh, A. G. Suppression of the Coffee-Ring Effect by Shape-Dependent Capillary Interactions. *Nature* **2011**, *476* (7360), 308−311.

(17) Bhardwaj, R.; Fang, X.; Somasundaran, P.; Attinger, D. Self-Assembly of Colloidal Particles from Evaporating Droplets: Role of DLVO Interactions and Proposition of a Phase Diagram. *Langmuir* **2010**, *26* (11), 7833−7842.

(18) Anyfantakis, M.; Geng, Z.; Morel, M.; Rudiuk, S.; Baigl, D. Modulation of the Coffee-Ring Effect in Particle/Surfactant Mixtures: The Importance of Particle−Interface Interactions. *Langmuir* **2015**, *31* (14), 4113−4120.

(19) Seo, C.; Jang, D.; Chae, J.; Shin, S. Altering the Coffee-Ring Effect by Adding a Surfactant-like Viscous Polymer Solution. *Sci. Rep.* **2017**, *7*, 1−9.

(20) Crivoi, A.; Duan, F. Elimination of the Coffee-Ring Effect by Promoting Particle Adsorption and Long-Range Interaction. *Langmuir* **2013**, *29* (39), 12067−12074.

(21) Soltman, D.; Subramanian, V. Inkjet-Printed Line Morphologies and Temperature Control of the Coffee Ring Effect. *Langmuir* **2008**, *24*, 2224−2231.

(22) Bou Zeid, W.; Brutin, D. Influence of Relative Humidity on Spreading, Pattern Formation and Adhesion of a Drying Drop of Whole Blood. *Colloids Surf., A* **2013**, *430*, 1−7.

(23) Patil, N. D.; Bange, P. G.; Bhardwaj, R.; Sharma, A. Effects of Substrate Heating and Wettability on Evaporation Dynamics and Deposition Patterns for a Sessile Water Droplet Containing Colloidal Particles. *Langmuir* **2016**, *32* (45), 11958−11972.

(24) Kim, D.-O.; Pack, M.; Rokoni, A.; Kaneelil, P.; Sun, Y. The Effect of Particle Wettability on the Stick-Slip Motion of the Contact Line. *Soft Matter* **2018**, *14* (47), 9599−9608.

(25) Still, T.; Yunker, P. J.; Yodh, A. G. Surfactant-Induced Marangoni Eddies Alter the Coffee-Rings of Evaporating Colloidal Drops. *Langmuir* **2012**, *28* (11), 4984−4988.

(26) Truskett, V. N.; Stebe, K. J. Influence of Surfactants on an Evaporating Drop: Fluorescence Images and Particle Deposition Patterns. *Langmuir* **2003**, *19*, 8271−8279.

(27) Shimobayashi, S. F.; Tsudome, M.; Kurimura, T. Suppression of the Coffee-Ring Effect by Sugar-Assisted Depinning of Contact Line. *Sci. Rep.* **2018**, *8* (1), 17769.

(28) Das, S.; Chakraborty, S.; Mitra, S. K. Ring Stains in the Presence of Electrokinetic Interactions. *Phys. Rev. E* **2012**, *85* (4), No. 046311.

(29) Marin, A.; Karpitschka, S.; Noguera-Marín, D.; Cabrerizo-Vílchez, M. A.; Rossi, M.; Kähler, C. J.; Rodríguez Valverde, M. A. Solutal Marangoni Flow as the Cause of Ring Stains from Drying Salty Colloidal Drops. *Phys. Rev. Fluids* **2019**, *4* (4), No. 041601.

(30) Misyura, S. Y. Evaporation of a Sessile Water Drop and a Drop of Aqueous Salt Solution. *Sci. Rep.* **2017**, *7* (1), 14759.

(31) Desarnaud, J.; Bonn, D.; Shahidzadeh, N. The Pressure Induced by Salt Crystallization in Confinement. *Sci. Rep.* **2016**, *6*, 30856.

(32) Shahidzadeh-Bonn, N.; Rafai, S.; Bonn, D.; Wegdam, G. Salt Crystallization during Evaporation: Impact of Interfacial Properties. *Langmuir* **2008**, *24* (16), 8599−8605.

(33) Müller-Steinhagen, H.; Malayeri, M. R.; Watkinson, a. P. Fouling of Heat Exchangers-New Approaches to Solve an Old Problem. *Heat Transfer Eng.* **2005**, *26* (1), 1−4.

(34) Schoenitz, M.; Grundemann, L.; Augustin, W.; Scholl, S. Fouling in Microstructured Devices: A Review. *Chem. Commun.* **2015**, *51* (39), 8213−8228.

(35) Mayer, M.; Bucko, J.; Benzinger, W.; Dittmeyer, R.; Augustin, W.; Scholl, S. Crystallization Fouling in Experimental Micro Heat Exchangers—Optical and Thermal Investigations. *Exp. Heat Transfer* **2013**, *26* (5), 487−502.

(36) Shahidzadeh, N.; Schut, M. F. L.; Desarnaud, J.; Prat, M.; Bonn, D. Salt Stains from Evaporating Droplets. *Sci. Rep.* **2015**, *5*, 10335.

(37) Kang, K. H.; Lim, H. C.; Lee, H. W.; Lee, S. J. Evaporation-Induced Saline Rayleigh Convection inside a Colloidal Droplet. *Phys. Fluids* **2013**, *25* (4), No. 042001.

(38) Zhong, X.; Ren, J.; Duan, F. Wettability Effect on Evaporation Dynamics and Crystalline Patterns of Sessile Saline Droplets. *J. Phys. Chem. B* **2017**, *121* (33), 7924−7933.

(39) Zhang, J.; Borg, M. K.; Sefiane, K.; Reese, J. M. Wetting and Evaporation of Salt-Water Nanodroplets: A Molecular Dynamics Investigation. *Phys. Rev. E - Stat. Nonlinear, Soft Matter Phys.* **2015**, *92*, 052403.

(40) Soulié, V.; Karpitschka, S.; Lequien, F.; Prené, P.; Zemb, T.; Moehwald, H.; Riegler, H. The Evaporation Behavior of Sessile Droplets from Aqueous Saline Solutions. *Phys. Chem. Chem. Phys.* **2015**, *17* (34), 22296−22303.

(41) Azimi, G.; Cui, Y.; Sabanska, A.; Varanasi, K. K. Scale-Resistant Surfaces: Fundamental Studies of the Effect of Surface Energy on Reducing Scale Formation. *Appl. Surf. Sci.* **2014**, *313*, 591−599.

(42) Picknett, R.; Bexon, R. The Evaporation of Sessile or Pendant Drops in Still Air. *J. Colloid Interface Sci.* **1977**, *61* (2), 336−350.

(43) Schönfeld, F.; Graf, K.-H.; Hardt, S.; Butt, H.-J. Evaporation Dynamics of Sessile Liquid Drops in Still Air with Constant Contact Radius. *Int. J. Heat Mass Transfer* **2008**, *51* (13), 3696−3699.

(44) Shanahan, M. E. R. Simple Theory of "Stick-Slip" Wetting Hysteresis. *Langmuir* **1995**, *11* (3), 1041−1043.

(45) Dietrich, E.; Kooij, E. S.; Zhang, X.; Zandvliet, H. J. W.; Lohse, D. Stick-Jump Mode in Surface Droplet Dissolution. *Langmuir* **2015**, *31* (16), 4696−4703.

(46) Baldwin, K. A.; Fairhurst, D. J. Classifying Dynamic Contact Line Modes in Drying Drops. *Soft Matter* **2015**, *11* (8), 1628−1633.

(47) Orejon, D.; Sefiane, K.; Shanahan, M. E. R. Stick−Slip of Evaporating Droplets: Substrate Hydrophobicity and Nanoparticle Concentration. *Langmuir* **2011**, *27* (21), 12834−12843.

(48) Hu, H.; Larson, R. G. Marangoni Effect Reverses Coffee-Ring Depositions. *J. Phys. Chem. B* **2006**, *110*, 7090−7094.

(49) Mullin, J. W. *Crystallization*, 4th ed.; Elsevier, 2001.

(50) De Yoreo, J. J.; Vekilov, P. G. Principles of Crystal Nucleation and Growth. *Rev. Mineral. Geochem.* **2003**, *54* (1), 57−93.

(51) de Gennes, P.-G.; Brochard-Wyart, F.; Quéré, D. *Capillarity and Wetting Phenomena: Drops, Bubbles, Pearls, Waves*; Springer, 2004.